Hindawi
Structural Control and Health Monitoring
Volume 2023, Article ID 5316136, 18 pages
https://doi.org/10.1155/2023/5316136

Research Article

Elastomagnetic Sensor-Based Long-Term Tension Monitoring of Prestressed Bridge Member with Temperature Compensation

Jooyoung Park,[1] **Won-Kyu Kim**,[2] **Kyo-Young Jeon**,[3] **and Seunghee Park**[4]

[1]*Department of the Civil, Architectural and Environmental System Engineering, Sungkyunkwan University, Suwon, Gyeonggi-do 16419, Republic of Korea*
[2]*Department of Convergence Engineering for Future City, Sungkyunkwan University, Suwon, Gyeonggi-do 16419, Republic of Korea*
[3]*Research Institute of Civil Engineering, Lotte E&C, Seoul 06515, Republic of Korea*
[4]*School of Civil, Architectural Engineering and Landscape Architecture, Sungkyunkwan University, Suwon, Gyeonggi-do 16419, Republic of Korea*

Correspondence should be addressed to Seunghee Park; shparkpc@skku.edu

Received 24 May 2023; Revised 13 August 2023; Accepted 17 November 2023; Published 11 December 2023

Academic Editor: Lucia Faravelli

Continuous monitoring of the prestressed members of a bridge under construction using the free cantilever method (FCM) is crucial for ensuring bridge safety. Temperature-sensitive sensors require special considerations as they may misinterpret the signal and tension. Moreover, the unnecessary and inappropriate use of features obtained from the sensor signal can deteriorate the efficiency of the signal and, therefore, tension analysis. This study proposes a tension estimation method using an embedded elastomagnetic (EM) sensor with a temperature-compensation technique. Changes in the signal due to the tension in the temporary steel rods were analyzed using a full-scale test, and the sensor data were acquired for 15 months via the field application. The temperature effect on the signal could be removed by subtracting the tension from the signal using the thermistor data, reducing the error by 91.99% when considering permeability. Additionally, linear regression (LR) and machine learning (ML) algorithms were adopted to predict the tension. Furthermore, the performances of both algorithms were compared using mean absolute error (MAE) and R^2. For the prediction using each feature in magnetic hysteresis, LR surpassed ML and the permeability exhibited the highest prediction performance. Meanwhile, predictions using multiple features were attempted to investigate the applicability of ML. Two cases of prediction were performed using ML: on using all the features and the other using three features excluding coercivity, which showed poor relevance to tension. As a result, the performance of the tension prediction was improved significantly compared to the results obtained by LR. In summary, the obtained results have demonstrated that the utilization of selective features of data with temperature compensation techniques could enhance predictive power.

1. Introduction

Free-cantilever method (FCM) is a bridge construction technique for superstructures that does not require the deployment of scaffolding systems. Temporary steel rods are used to attach the upper girder to the pier to provide resistance against imbalanced forces generated when one girder is longer than the other.

In 2016, as shown in Figure 1, the Chilsan Bridge tilted during construction and collapsed while the segments were connected [1]. The bridge collapsed primarily because it could not withstand the tensile stress generated during the concrete pouring of the last segment. The generated tensile stress disjointed the steel rods fastened by the coupling and separated the pier and head of the bridge. The overturning and collapse of the girder could have been prevented if the tension applied to the temporary steel rod had been examined in real time.

Generally, instruments such as accelerometers, strain gauges, fiber Bragg grating (FBG) sensors, lead zirconate titanate (PZT) sensors, and elastomagnetic (EM) sensors are used to monitor the tension of prestressed members in civil

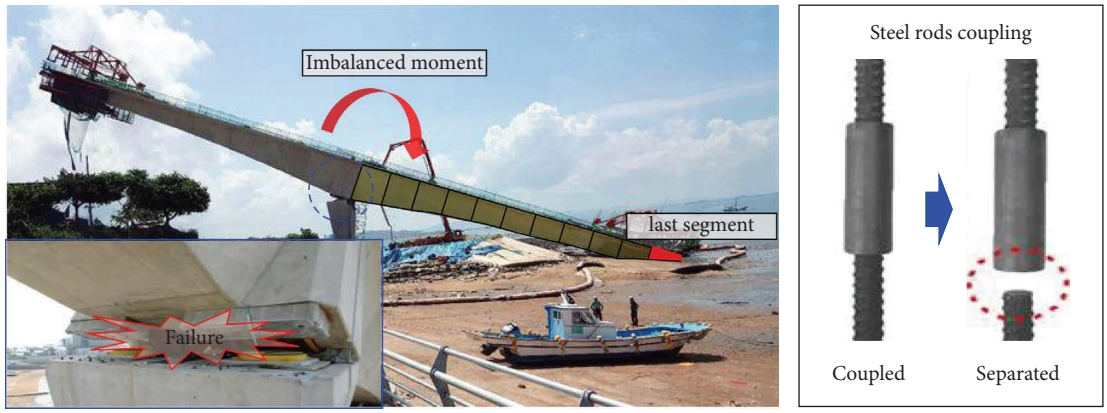

Figure 1: Collapse of Chilsan Bridge (2016) under construction. Images reproduced from an article by Gyeongwoo park, the hankook ilbo [1].

structures. The cable tension estimation in cable-stayed bridges has mainly been performed using contact-based measurement techniques with accelerometers, and there are several related studies [2–6]. By obtaining the dynamic characteristics from the modal frequency using accelerometers installed on the cable, the proposed formula for cable tensile force estimation can be applied to calculate the cable tension of a cable-stayed bridge; the relation between the cable tension and vibration data was verified using the dependency of the acceleration data on cable vibration. Subsequently, studies were conducted using noncontact-based laser Doppler vibrometers (LDV) and radar devices [7, 8]. Furthermore, computer vision-based measurement systems have been utilized recently [9, 10]. A noncontact, video-based method that uses image-processing techniques, phase-based motion estimation, short-time Fourier transform (STFT), and taut-string theory was proposed to isolate cable vibrations from camera movement and calculate real-time tension. These methods have been confirmed to exhibit acceptable accuracy in structural health monitoring of cable-stayed bridges through field application. However, it is difficult to manage the tension of prestressed members embedded inside, such as steel strands or rebars.

For tension monitoring of prestressed concrete (PSC) girders or reinforced concrete (RC) beams, FBG, PZT, and EM sensors are primarily used. The FBG sensor detects physical properties such as tension via a change in the reflected light spectrum of the Bragg grating inside an optical fiber varying with strain and temperature. Hence, it allows for precise measurement and achieves accuracy with a relative error of less than 3% [11]. However, implementing the FBG requires modification of the central wire of the strand to insert the optical fiber, which can be highly susceptible to damage under high load conditions. Tension management was also performed using a PZT interface, which detected variations in prestress forces by measuring changes in the electromechanical impedance response resulting from alterations in the stress field and contact parameters of the tendon anchorage [12]. However, this method indirectly estimates the tension by detecting changes in contact force and stress field between the anchor block and the bearing plate, unlike the accelerometer applied to the cable. This makes it difficult to estimate the tensile stress occurring in the material directly.

The EM sensor, a noncontact sensor that is not directly coupled to the tension member, can be either embedded in or installed outside the structure to estimate the tension of the prestressed member, marking the first application of this method to bridge cables [13]. While load cells must undergo equipment calibration every 1 to 2 years, EM sensors are inexpensive to fabricate and can be used during both the construction and maintenance phases. Studies have used embedded EM sensors to estimate the tension of prestressed (PS) tendons inside PSC girders [14, 15]. These studies predicted the tension using the permeability or the area of the magnetic hysteresis curve and showed that as the tension increases, the permeability and area decrease. However, depending on the inherent material and magnetic properties of the ferromagnetic specimen, the relationship between tension and permeability can either be inversely proportional or directly proportional [16, 17].

During the construction phase of the bridge using FCM, steel rods with large diameters such as 40 mm or larger are used as prestressed members. Furthermore, there is only one study analyzing the difference in induced voltage signals according to the change in tension between them [18]. However, the relationship between the features of magnetic hysteresis and environmental factors such as temperature was not analyzed theoretically. In other words, signal changes due to temperature changes during long-term monitoring were not considered though the result of tension estimation using EM sensors had practical accuracy. A few studies have considered the temperature for tension estimation using stress-measurement sensors based on a polynomial fitting method or artificial intelligence (AI) [12, 18–20]. Because the studies were performed under specific temperature conditions, variations in temperature from a long-term perspective were only partially considered. Therefore, the results may not be reliable because the temperature and force-related data were fitted without identifying the effect of the temperature analytically [18, 20]. Moreover, if artificial neural networks (ANNs) are used

without analyzing the effect of temperature properly, the number of training patterns, that is, the number of observations, can adversely affect the results [12].

Meanwhile, using machine learning (ML) is advantageous for prediction with various data features and has been widely used in structural health monitoring [21]. The results were satisfactory for predicting the target values in previous studies [22, 23]. However, a question remains as to whether ML should be applied to the prediction of tension using the EM sensor data. This is because the relationship between the used features of the hysteresis curve and the tension was derived almost linearly in previous studies [13–15, 18–20, 24]. Therefore, it is necessary to compare the results obtained using ML to those obtained using a simple regression method when predicting tension. Accordingly, the applicability of ML should be subsequently analyzed by establishing if the prediction performance improves when utilizing various characteristics of the hysteresis curve properly.

This study proposes a long-term tension monitoring method for temporary steel rods as prestressed members using an embedded EM sensor through field application to a bridge under construction. First, a theoretical analysis was performed using a magnetic hysteresis model about the stress in the ferromagnetic material. Subsequently, the change in the magnetic hysteresis due to the tension was analyzed by conducting a full-scale test before the field application. Then, the effect of temperature on the EM sensor signal was examined logically and compensated using the full-scale test and field application data. A linear regression (LR) model was used for tension prediction, and an appropriate ML model was adopted for comparison. Finally, both models were compared using evaluation metrics, and the applicability of the ML model was investigated.

2. Methodology

2.1. Embedded Elastomagnetic (EM) Sensor. An EM sensor consists of primary and secondary coils. A magnetic field develops inside the ferromagnetic core in the longitudinal direction when a voltage is applied to the primary coil [13]. The developed magnetic field induces a voltage in the secondary coil based on Faraday's law. Therefore, the magnetic flux density can be calculated by measuring the induced voltage using an EM sensor. Figure 2 shows the architecture of the embedded EM sensor.

The EM sensor has both primary and secondary coils. The magnetic field strength H (or magnetizing field) generated by the primary coil is expressed as

$$H = \mathrm{NI}, \tag{1}$$

where N and I represent the number of primary coil windings (turns/m) and current (A) applied to the primary coil (A), respectively. An electromotive force is induced in the secondary coil when current I is generated by the voltage flow through the primary coil, and it is expressed according to Faraday's law as

$$e_2(t) = -N_2 \frac{d\Phi_{21}(t)}{\mathrm{d}t}, \tag{2}$$

where Φ_{21} (t) denotes the magnetic flux induced by the primary coil of the secondary coil and N_2 is the number of the secondary coil windings (turns/m). The magnetic flux density was obtained by dividing the inner area of the coil by the magnetic flux flow. The magnetic flux density B is expressed as

$$B = \mu(H + M), \tag{3}$$

where μ is the magnetic permeability and M is the magnetization vector field that expresses the induced magnetic dipole moments in the material. Because M is extremely small in air, the magnetic flux density has a linear relation with magnetic field strength. However, it changes under stress owing to magnetomechanical effects [25].

2.2. Magnetization of Ferromagnetic Material under Stress. A magnetic field was induced inside the sensor coil, and the ferromagnetic material was magnetized when an AC voltage was applied to the primary coil surrounding the ferromagnetic material. However, if a ferromagnetic material is subjected to a constant stress, the magnetization does not follow the original curve and takes a new path, as indicated by the dashed line in Figure 3.

The variation in the magnetization dM can be positive or negative, depending on the induced stress sign and the material property. Magnetization M comprises irreversible and reversible components according to the Jiles–Atherton magnetic hysteresis model [27].

$$\begin{aligned} M &= M_{\mathrm{rev}} + M_{\mathrm{irr}} \\ &= c\left(M_{\mathrm{an}} - M_{\mathrm{irr}}\right) + M_{\mathrm{irr}}, \end{aligned} \tag{4}$$

$$\begin{aligned} M_{\mathrm{an}} &= M_s\left(\coth\left(\frac{H_e}{a} - \frac{a}{H_e}\right)\right), \\ H_e &= H + \alpha M + H_\sigma. \end{aligned} \tag{5}$$

In equation (4), M_{rev} represents the reversible magnetization, M_{irr} represents the irreversible magnetization, and c represents the reversible magnetic susceptibility. In equation (5), M_{an} is the anhysteretic magnetization related to the M_{rev}, M_s is the saturation magnetization, a is the domain density, and α is the domain coupling factor. Reversible magnetization is caused by the bending of the domain wall, and irreversible magnetization is caused by the displacement of the magnetic domain [28]. The effective field H_e, which has a stress-related term H_σ, changes depending on the variation in the mechanical stress in the ferromagnetic material. Moreover, the parameters c, a, α, and others, which were examined in other studies by several researchers [25, 29, 30], change owing to the residual stress in the ferromagnetic material, making the total magnetization different. Therefore, if a steel rod as a ferromagnetic material is under tension, reversible and irreversible magnetization occurs, causing changes in the properties of magnetic hysteresis.

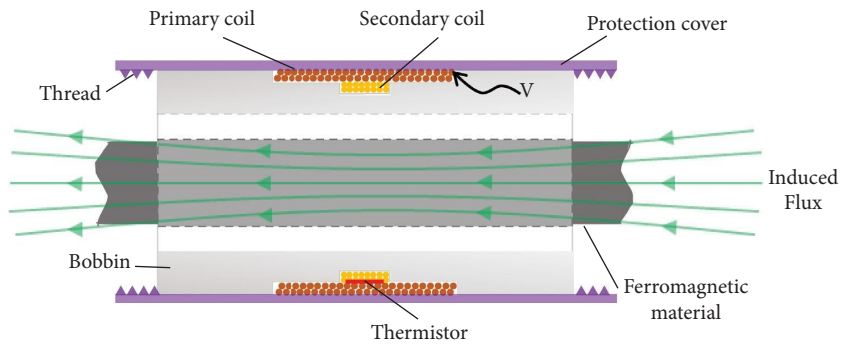

Figure 2: Architecture of EM sensor. Image reproduced from Sumitro et al. [24].

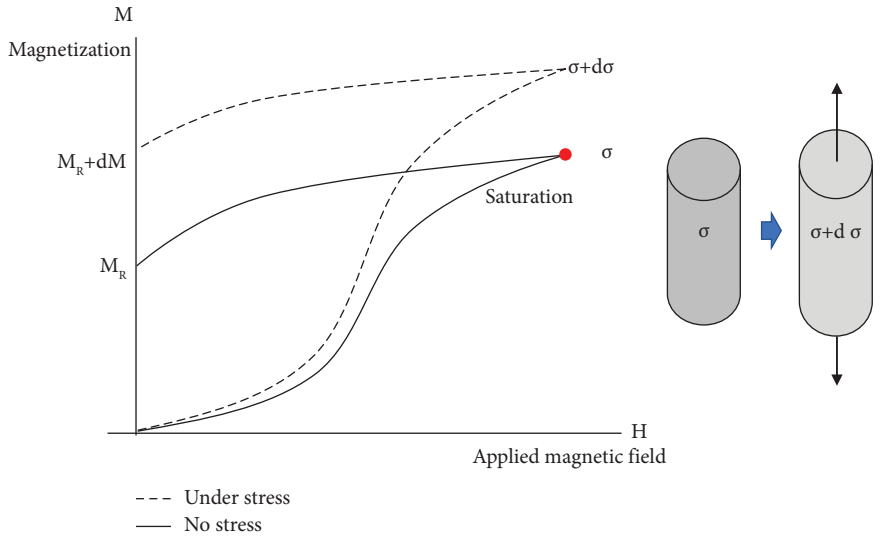

Figure 3: Variation of the magnetic hysteresis curve caused by the stress state. Image reproduced from Markar and Tanner [26].

2.3. Feature Extraction from Magnetic Hysteresis Curve. Figure 4 shows the extracted coercivity and retentivity through the relation between the magnetizing force and magnetic flux density of the magnetic hysteresis curve generated when a sinusoidal voltage is applied to the EM sensor coil.

The area and permeability were determined from the geometry of the hysteresis curve. Coercivity is defined as the magnetizing field when M is 0, and retentivity is defined as the magnetization when H is 0.

2.4. Tracing Temperature Change on Embedded EM Sensor Using Thermistor. A thermistor is a sensor made of semiconductor materials and operates on the principle that resistance varies with temperature [31]. Negative (NTC) and positive temperature coefficient (PTC) thermistors are the two types of thermistors used. In the case of an NTC-type thermistor, the resistance decreases with an increase in temperature, while the resistance increases with an increase in temperature in a PTC-type thermistor.

The sensing parts of the embedded EM sensor are composed of copper coils that are sensitive to temperature changes, implying that the resistance of the coils is altered depending on the external environment [32]. For example, the magnetic hysteresis of a ferromagnetic material with identical tensile stress may be measured differently owing to temperature variations, even though it has the same material properties. Consequently, the resistance must be measured to interpret the EM sensor signals accurately when the temperature fluctuates day and night over a long period.

The thermistor was used as a sensor to obtain temperature-related resistance by attaching it to the surface of the target material. The change in the signal obtained from the EM sensor is attributed to the resistance of the coil, which changes with the temperature or the difference in the current that accompanies it.

2.5. Tension Estimation. The relation between the raw data from the EM sensor and the stress in the temporary steel rod is complex, and there is no theoretical formula to express this relationship. Thus, it is necessary to use LR analysis or ML to predict the material tension.

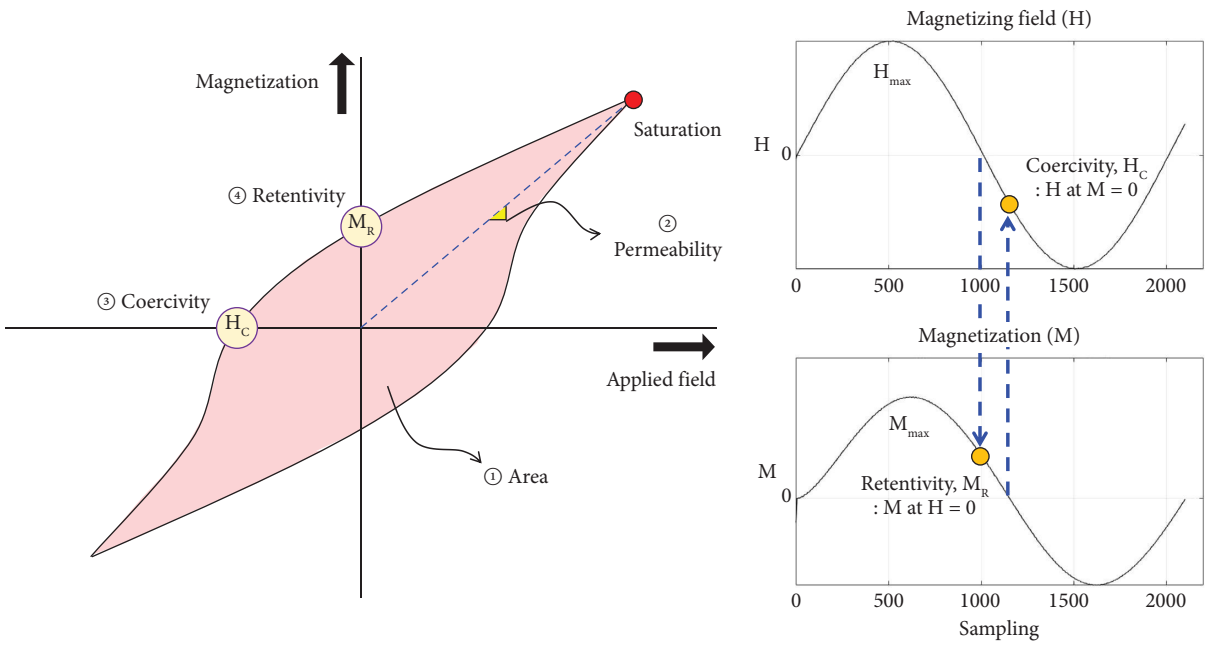

Figure 4: Feature extraction from the magnetic hysteresis curve.

First, a full-scale test was conducted to estimate the tension of temporary steel rods in the field application, and the obtained data were analyzed using the aforementioned algorithms. For the LR, a linear regression analysis was performed to fit the extracted features of the magnetic hysteresis curve to the tension measured by a load cell. The developed relational expressions were then used to calculate the tension of temporary steel rods in field applications.

For tension prediction using a ML model, the open library provided by PyCaret (v. 3.0.0) was utilized. Figure 5 shows the process to select a proper ML model for tension prediction and its configuration.

After temperature compensation and the hysteresis curve, the extracted features are input into the ML models provided by PyCaret. The ML models used for evaluation include tree-based models such as Extra Trees (ET), Random Forest (RF), and Decision Tree (DT), Boosting models such as Gradient Boosting Regressor (GBR), Light Gradient Boosting Machine (LightGBM), Extreme Gradient Boosting (XGBoost), and CatBoost, and linear models such as Ridge Regression (Ridge) and others. The k-fold cross-validation method was employed for training and validation. In this method, the dataset is divided into k subsets and the model is trained k times, each time using k-1 subsets for training and the remaining subset for validation [33]. The average performance of each model is determined by a designated evaluation metric during the cross-validation. In this study, the cross-validation results of the top three performing models are compared to select the best model ultimately. After selecting the best model, a Bayesian search algorithm that explores a new combination of hyperparameters at each iteration and seeks the optimal hyperparameters based on previous results is utilized to optimize the evaluation metric [34].

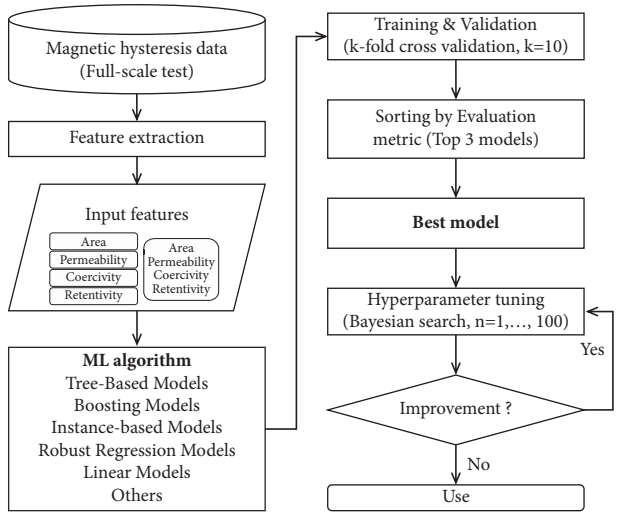

Figure 5: Application process and configuration of the ML model.

Hyperparameter tuning is carried out for up to 100 iterations and adopts current hyperparameters if there is no further performance improvement.

Data obtained from the field application are input into two established algorithms to compare the predictive force for each feature. To assess the ML application, the prediction performance for a case where all features are input to the ML model is analyzed. Finally, the effectiveness of selective feature use is examined, and the applicability of ML to EM sensor data is discussed.

2.6. Model Evaluation. The analysis models obtained by the LR and ML were assessed using the mean absolute error (MAE) and R-squared (R^2).

$$\mathrm{MAE} = \frac{1}{n}\sum_{i=1}^{n}\left|y_{i,\mathrm{ref}} - y_{i,\mathrm{pred}}\right|,$$
$$R^2 = 1 - \frac{\sum\left(y_{i,\mathrm{ref}} - y_{i,\mathrm{pred}}\right)^2}{\sum\left(y_{i,\mathrm{ref}} - \overline{y}_{i,\mathrm{ref}}\right)^2}, \quad (6)$$

where $y_{i,\mathrm{ref}}$ and $y_{i,\mathrm{pred}}$ represent the reference values of the load cell and the values predicted by the estimation model, respectively. The MAE evaluates the absolute distance between the tension by the load cell and the response from the model considering negative errors. In contrast, R^2 is a statistical measure that represents the explanatory power of the regression analysis model. This value generally ranges from 0 to 1 when using training data, with values closer to 1 indicating that the model explained the variability of the data well. However, R^2 can be negative when new data are used, which leaves the possibility that used that feature should be discarded.

3. Field Application

3.1. Full-Scale Test. As shown in Figure 6, a full-scale test was conducted to verify the field applicability of the EM sensors *a priori* application at the construction site. The primary and secondary coils of the EM sensor with a diameter of 1.2 and 0.2 mm were wound with 300 and 180 turns, respectively. Additionally, an NTC-type thermistor (SA1-TH-44004-40-T, Omega) was attached between the primary and secondary coils to obtain temperature-related data. The inner face of the embedded EM sensor bobbin is connected to a sheath thread around the steel rod.

For the measurement, the embedded EM sensors were connected through a data transmission cable to a data acquisition (DAQ) device, and the signal amplifier was incorporated into a controlling desktop PC using LabVIEW software (v. 19.0). For the DAQ device, a National Instrument (NI) USB-6212 was adopted, which had two 16 bit analog output channels: 250E3 Samples/s and ±10 V an output range. A sinusoidal alternating current signal of ±3 V at 1 Hz was input through the coils of the EM sensors. A vibrating wire-type load cell (SJ-3000) with a capacity of 120 tons was used with sensors to measure tension as a reference value.

A full-scale test was conducted to test the sensors that would be installed on temporary steel rods with a design prestressing force of 60 and 64 tons for on-site applications. Two sensors and two concrete specimens were used, and each sensor was embedded in a single specimen for the measurement. The specimen for sensor 1 was gradually prestressed from 18.26 to 66.52 tons, and the specimen for sensor 2 was prestressed from 21.88 to 70.82 tons. Figure 7 shows the magnetic hysteresis curves measured at each load step.

First, both curves exhibit a steepening of the corresponding closed curve towards the y-axis as the tension increases, and the area of the curve gradually increases. Additionally, as the tension increases, the remaining magnetization in the temporary steel rods increases despite removing the magnetic field and the coercivity required to eliminate the residual magnetization increases slightly.

Table 1 presents the numerical changes in the magnetizing field and the maximum magnetization of the steel rod, along with the rate of change for the initial loading step, as the load increases. The change in the magnetizing field with the increase in load was found to be negligible, showing changes within 0.71% of the value when the load was 21.88 tons, as in the case of sensor 2. The magnetization, however, increased by up to 36.26% for sensor 2 compared with the lowest load. In Figure 8, four features of the magnetic hysteresis curve were extracted and examined for each load step.

Four features of the magnetic hysteresis curve were extracted and examined for each load step, all of which showed a positive correlation with an increase in the load. When conducting long-term monitoring after on-site application, the range in which the tension introduced into temporary steel rods varied was very narrow, and it was found that the number of features within that range was insufficient to derive a relation with the tension. Therefore, it was necessary to interpolate the full-scale test data after identifying the changing tension range and the size of data acquired during on-site monitoring. This will be addressed after presenting the results of the on-site applications.

3.2. Field Application of EM Sensor. An experimental study was conducted using FCM on the Jusangcheon Bridge, a bridge under construction in Buan-gun, Jeollabuk-do, South Korea. The Jusangcheon Bridge is an extradosed bridge with a PSC box girder having a length and width of 210 and 30 m, respectively. Figure 9, a construction site photograph and a drawing provided by Lotte E&C, shows the location of the EM sensors on the pier head.

During construction, steel rods of lengths 10.47 and 9.47 m with a diameter of 40 mm were embedded, and the EM sensor was installed on the shorter ones located at the edge of the pier head, as shown in Figure 10(a). Two EM sensors with the same specifications as those in the full-scale test were embedded in the pier table for measurements in field applications. The steel rod with sensor 1 was prestressed to a design load of 60 tons, and the steel rod with sensor 2 was prestressed to a design load of 64 tons. The EM sensor signals were measured to estimate the tension of the temporary steel rods at 30-min intervals for approximately 15 months from October 2020 to February 2022, except when the on-site power supply was cut off.

3.3. Measurement Results. Load cells were installed on-site to measure the tension of the temporary steel rods to secure the main pier and pier table, as shown in Figure 10(b), and data were acquired along with the installed EM sensors. A total of 10,954 data were obtained from the EM sensors and load cells during the measurement period. The area, permeability, coercivity, and retentivity extracted from the data of the two EM sensors over the approximately 15-month

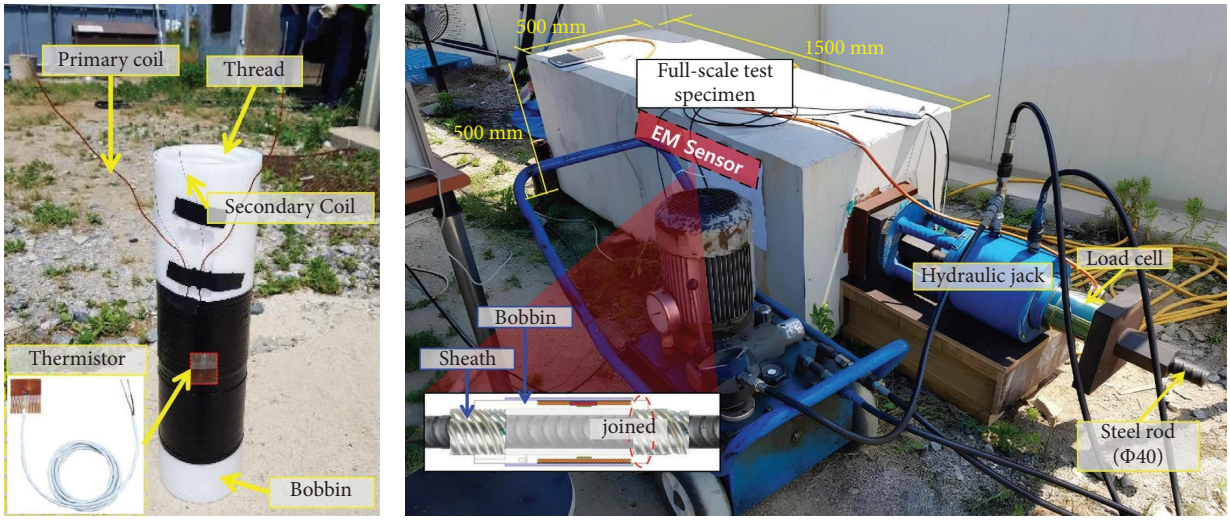

Figure 6: Setup and components of the full-scale test. (a) Composition of EM sensor. (b) Full-scale test setup.

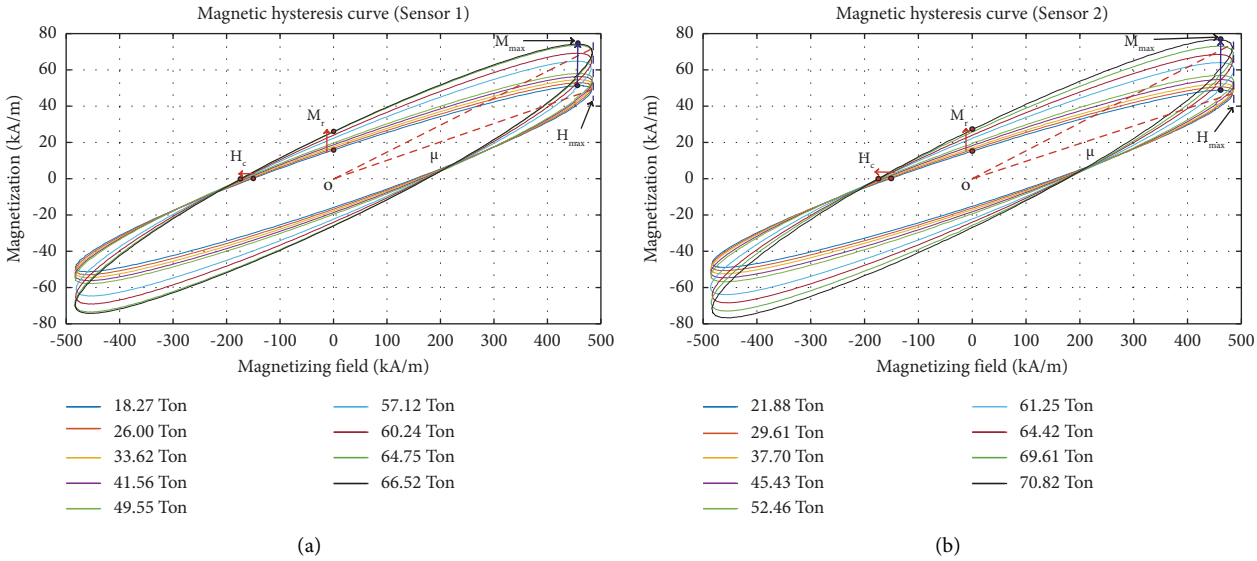

Figure 7: Property changes of the magnetic hysteresis curve according to prestressing force. (a) Magnetic hysteresis curve obtained from sensor 1. (b) Magnetic hysteresis curve obtained from sensor 2.

Table 1: Numerical analysis of full-scale test results.

	Sensor 1					Sensor 2			
Load (ton)	H_{max} (kA/m)	Δ (%)	M_{max} (kA/m)	Δ (%)	Load (ton)	H_{max} (kA/m)	Δ (%)	M_{max} (kA/m)	Δ (%)
18.26	482.92	—	51.31	—	21.88	483.20	—	48.90	—
26.00	482.99	0.01	52.99	3.17	29.61	484.66	0.30	50.65	3.46
33.62	483.66	0.15	54.69	6.18	37.70	486.12	0.60	52.43	6.73
41.56	483.93	0.21	56.37	8.98	45.43	486.09	0.59	54.69	10.59
49.55	484.50	0.33	58.05	11.61	52.46	486.06	0.59	56.96	14.15
57.12	481.97	−0.20	64.84	20.87	61.25	486.65	0.71	64.02	23.62
60.24	482.80	−0.02	69.23	25.88	64.42	483.45	0.05	68.56	28.68
64.75	484.55	0.34	73.63	30.31	69.61	485.24	0.42	73.11	33.11
66.52	484.18	0.26	74.23	30.88	70.82	484.11	0.19	76.72	36.26

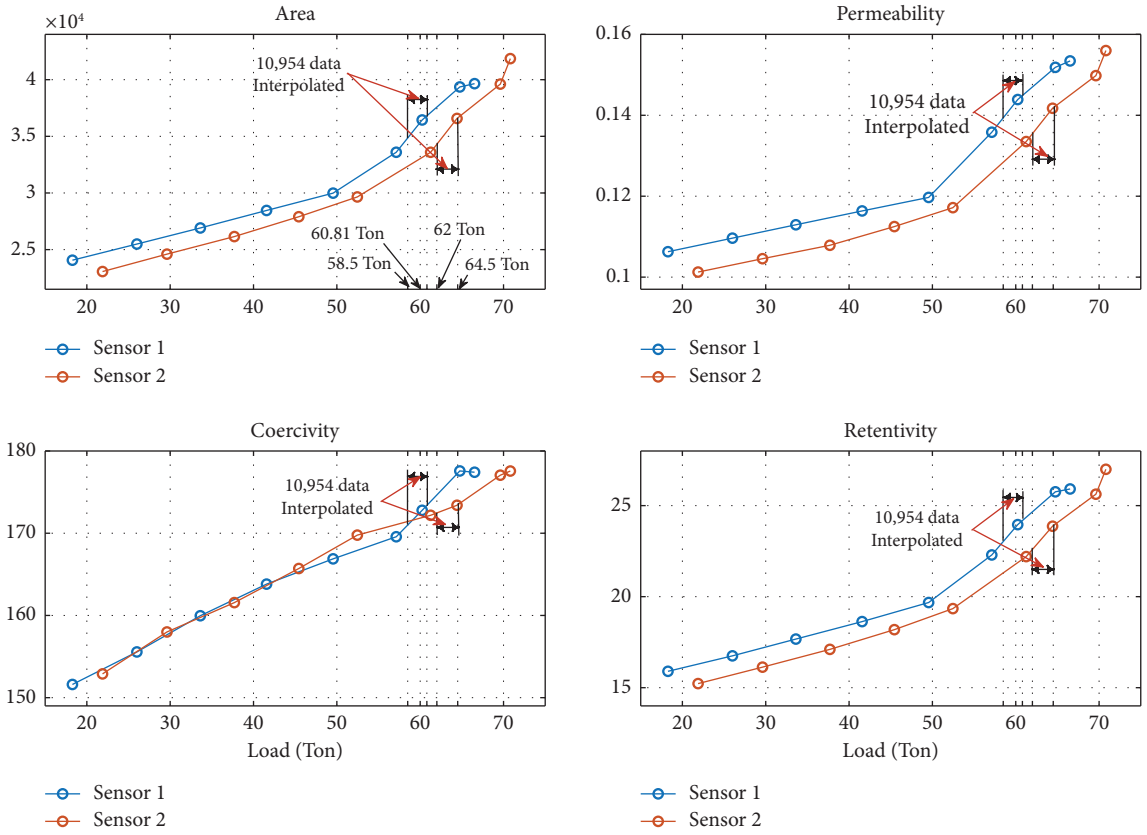

Figure 8: Feature changes of the magnetic hysteresis curve.

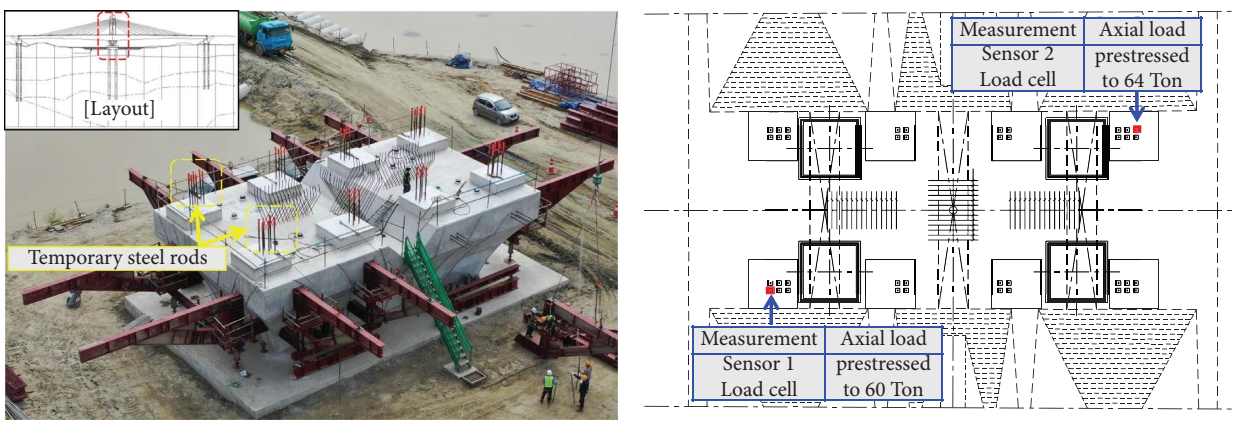

Figure 9: Site view of the field application and EM sensors' location. Images reproduced with permission from Lotte E&C. (a) Main pier of the Jusangcheon Bridge under construction. (b) Location of EM sensors and applied prestressed force in temporary steel rods.

measurement period are shown in Figure 11, and the load cell data are shown in Figure 12.

The initial tension when the load cells began measuring with the EM sensors was 59.7 and 63.6 tons for the temporary steel rods where sensor 1 and sensor 2 were installed, respectively. As the temperature decreased, the tension gradually increased to approximately 60.8 and 64.5 tons by the end of January. This showed a low change rate of approximately 2%, and the alteration in the tensile stress came from the contraction of the material caused to the change in the thermal expansion coefficient of the temporary steel rods.

All features, excluding the permeability, increased with the tension in the temporary steel rods. However, considering the positive correlation between tension and permeability in the results of the full-scale test in Figure 8, the permeability extracted from magnetic hysteresis data of sensors 1 and 2 exhibited an opposite

Figure 10: Installation of EM sensors and load cell. (a) Installation of EM sensor. (b) Prestressing and load cell.

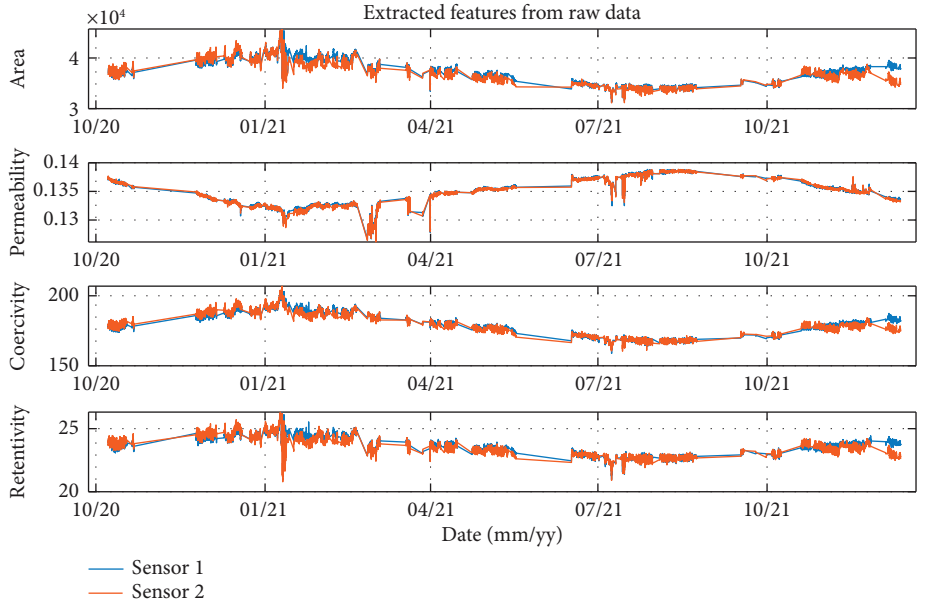

Figure 11: Measured and extracted features from the magnetic hysteresis curves.

trend, as shown in Figure 11. This indicates that the characteristics of the sensor coil owing to temperature changes and the significant changes in temperature during the long-term monitoring of the sensor affected the output signal. Although the other features had the same tendencies as the full-scale test results, their magnitudes may have been different. Therefore, as mentioned earlier, it is necessary to eliminate the temperature effect on the output signal.

3.4. Temperature Compensation Method. The resistance of the thermistor (R), magnetizing field (H), magnetization (M), and load cell values were compared to eliminate the influence of temperature on the EM sensor. H did not change significantly as the tension increased in the full-scale experiment; therefore, it was found to be affected only by temperature. M is affected by the tensile stress of the specimen, according to the theory of the magneto-mechanical effect [25], and temperature, which changes the

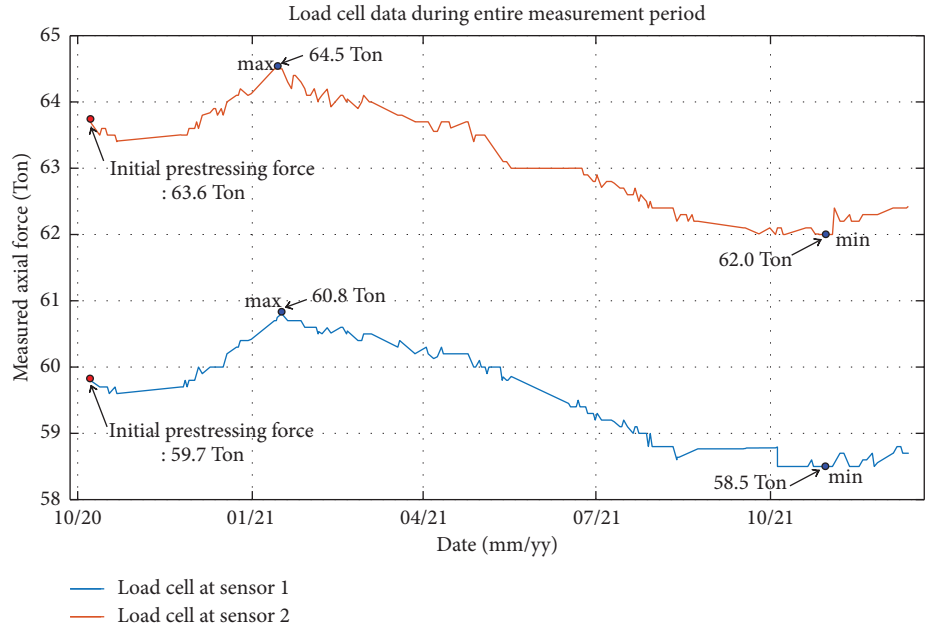

FIGURE 12: Load cell data during the entire measurement.

physical characteristics of the copper coil. Therefore, the influence of temperature can be removed for each data point using the relations between the mentioned values, as shown in Figure 13.

First, the average resistance of the thermistor measured in the full-scale test was 1006 Ω, and a specific resistance value showing the most identical value to it was selected. Among the 10,954 data points, the 6,719th measurement was almost similar at 1006.6 Ω. The H_{peak}, M_{peak}, and load cell values at this point were used as reference values for the values at other data points, which were relative to the reference values. The relative values were calculated by dividing the original value of each data point by the value at the reference point, and the differences between each value and the reference values were derived as follows:

$$\begin{aligned}
\Delta\left(H_{\mathrm{rel,peak}}, M_{\mathrm{rel,peak}}, L_{\mathrm{rel}}\right)(t) &= \left(H_{\mathrm{rel,peak}}, M_{\mathrm{rel,peak}}, L_{\mathrm{rel}}\right)(t) - \mathbf{1}, \\
\begin{pmatrix} \Delta H_{\mathrm{rel,peak}}(t) \\ \Delta M_{\mathrm{rel,peak}}(t) \\ \Delta L_{\mathrm{rel}}(t) \end{pmatrix} &= \begin{pmatrix} H_{\mathrm{rel,peak}}(t) - \mathbf{1} \\ M_{\mathrm{rel,peak}}(t) - \mathbf{1} \\ L_{\mathrm{rel}}(t) - \mathbf{1} \end{pmatrix}, \\
H_{\mathrm{compensated}} &= \left(\mathbf{1} - \Delta H_{\mathrm{rel,peak}}(t)\right) \times H_{\mathrm{orig}}^{T} \\
M_{\mathrm{compensated}} &= \left(\mathbf{1} - \left(\Delta M_{\mathrm{rel,peak}}(t) - \Delta L_{\mathrm{rel}}(t)\right)\right) \times M_{\mathrm{orig}}^{T}(t),
\end{aligned} \tag{7}$$

where $H_{\mathrm{rel,peak}}$, $M_{\mathrm{rel,peak}}$, and L_{rel} represent the relative values of the peak magnetizing field, peak magnetization, and load cell, respectively. H_{orig} and M_{orig} are the original values of the magnetizing field and magnetization, respectively, and $H_{\mathrm{compensated}}$ and $M_{\mathrm{compensated}}$ are the temperature-compensated values. The results of temperature compensation are shown in Figure 14.

Using the proposed temperature compensation method, the effects of temperature on the magnetizing field (H) and magnetization (M) of each sensor were removed. The fluctuating tendencies of all features were significantly eliminated, leaving only the effects of stress changes in the temporary steel rods. For permeability, the trends before and after temperature compensation differ; the value decreases as the stress increases before compensation, whereas the two values are proportional after compensation. Because the trend became consistent with the data obtained during the full-scale test when the temperature was constant, it was found that the proposed method of eliminating temperature effects was effective.

3.5. Tension Prediction by Linear Regression and Extra Trees (ET). The full-scale test section confirmed that it is necessary to interpolate the data to derive the relation between the stress and the four features extracted from the magnetic hysteresis data. The number of EM sensor data acquired

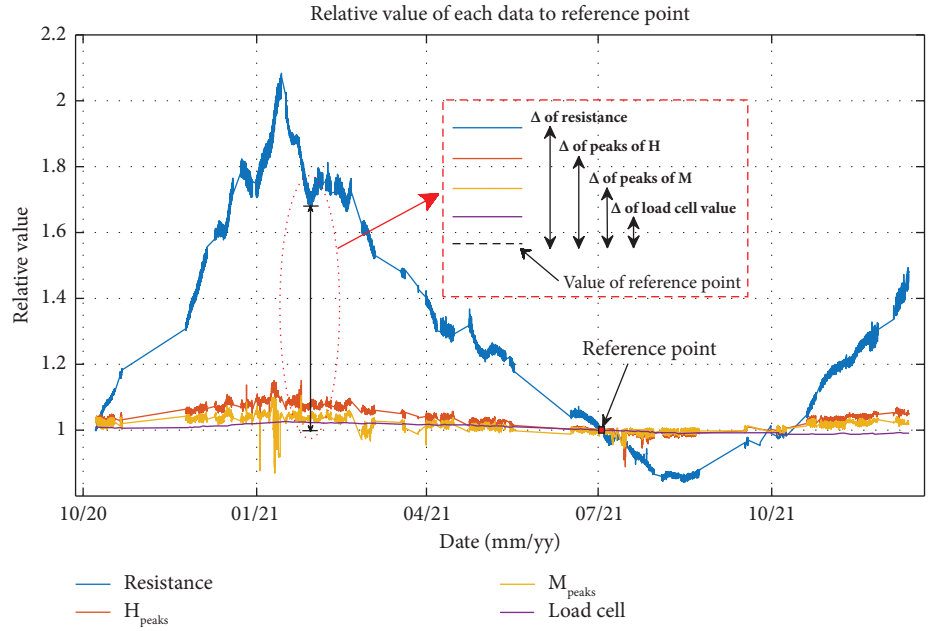

Figure 13: Description of temperature compensation and relative data values to the reference point.

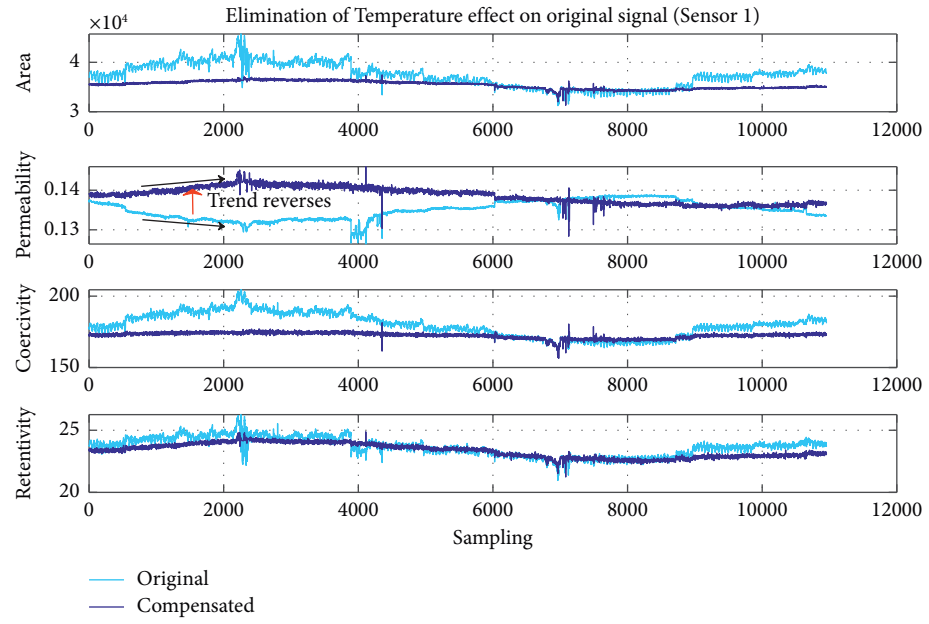

(a)

Figure 14: Continued.

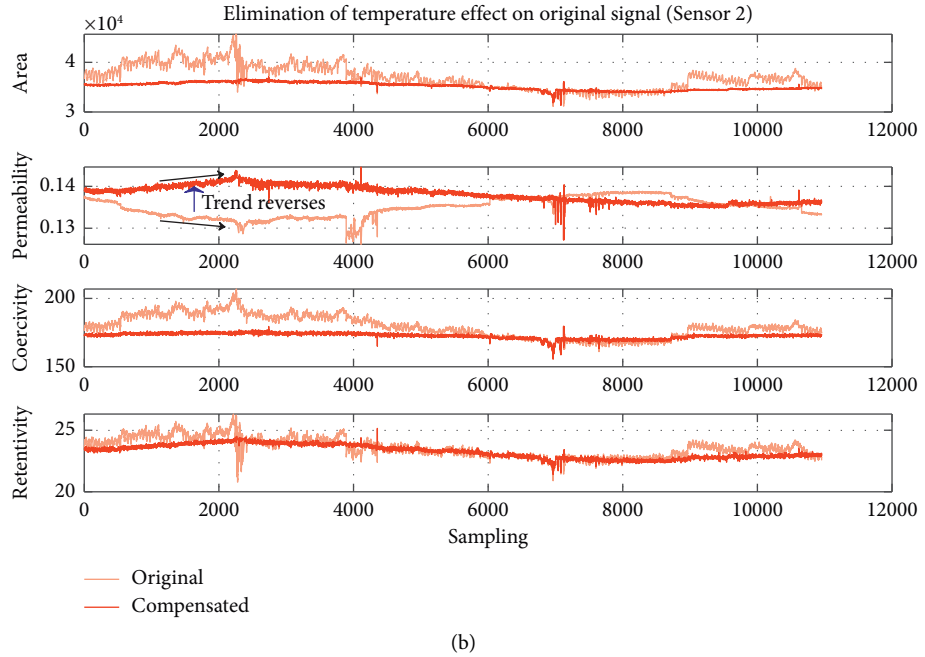

(b)

Figure 14: Temperature compensation results of extracted features from the magnetic hysteresis curve. (a) Features of the magnetic hysteresis curve after temperature compensation (sensor 1). (b) Features of the magnetic hysteresis curve after temperature compensation (sensor 2).

Table 2: Relation between each feature and tension through LR analysis.

Feature	Sensor 1	Sensor 2
Area	$0.001148 \times \text{Area}_{s1} + 18.47$	$0.001065 \times \text{Area}_{s2} + 25.49$
Permeability	$406.6 \times \text{Permeability}_{s1} + 3.363$	$386.3 \times \text{Permeability}_{s2} + 9.675$
Coercivity	$0.9631 \times \text{Coercivity}_{s1} - 106.2$	$2.564 \times \text{Coercivity}_{s2} - 380.2$
Retentivity	$1.951 \times \text{Retentivity}_{s1} + 13.54$	$1.904 \times \text{Retentivity}_{s2} + 18.98$

Table 3: Cross-validation and test results using full-scale datasets and derived hyperparameters.

Category		Extra trees (ET)		Random forest (RF)		Gradient boosting regression (GBR)	
		MAE (ton)	R^2	MAE (ton)	R^2	MAE (ton)	R^2
Sensor 1	Validation	0.0026	0.9921	0.0043	0.9793	0.0094	0.9838
	Test	0.0006	0.9992	0.0028	0.9867	0.0105	0.9570
Sensor 2	Validation	0.0025	0.9844	0.0032	0.9772	0.0085	0.9825
	Test	0.0065	0.9373	0.0089	0.8908	0.0123	0.9371
Tuned hyperparameter		Max_features: 1.0, min_samples_leaf: 1, min_samples_split: 2, n_estimators: 100		Bootstrap: true, max_features: 1.0, min_samples_leaf: 1, min_samples_split: 2, n_estimators: 100		Max_features: 1.0, min_impurity decreases: $1e-09$, min_samples_leaf: 1, min_samples_split: 10, n_estimators: 300	

during the monitoring period was 10,954, and the prestressing force change ranges of the temporary steel rods at sensor 1 and sensor 2 were 58.5 to 60.8 tons and 62.0 to 64.5 tons, respectively, as shown in Figure 12. It was assumed that each feature changed linearly within the prestressed force-changing range, and interpolation was performed using all data. Table 2 shows the equations for the relation between the features and prestressed force (tons) of sensors 1 and 2 obtained from the LR analysis for the corresponding changes in the force.

Because the magnetic hysteresis curve contains several features, it is necessary to consider the changes in all features in tension prediction using an ML algorithm. To select an appropriate ML algorithm, 10,954 interpolated data from the full-scale test were input into all the ML models provided by PyCaret (v.3.0.0) open library, and the

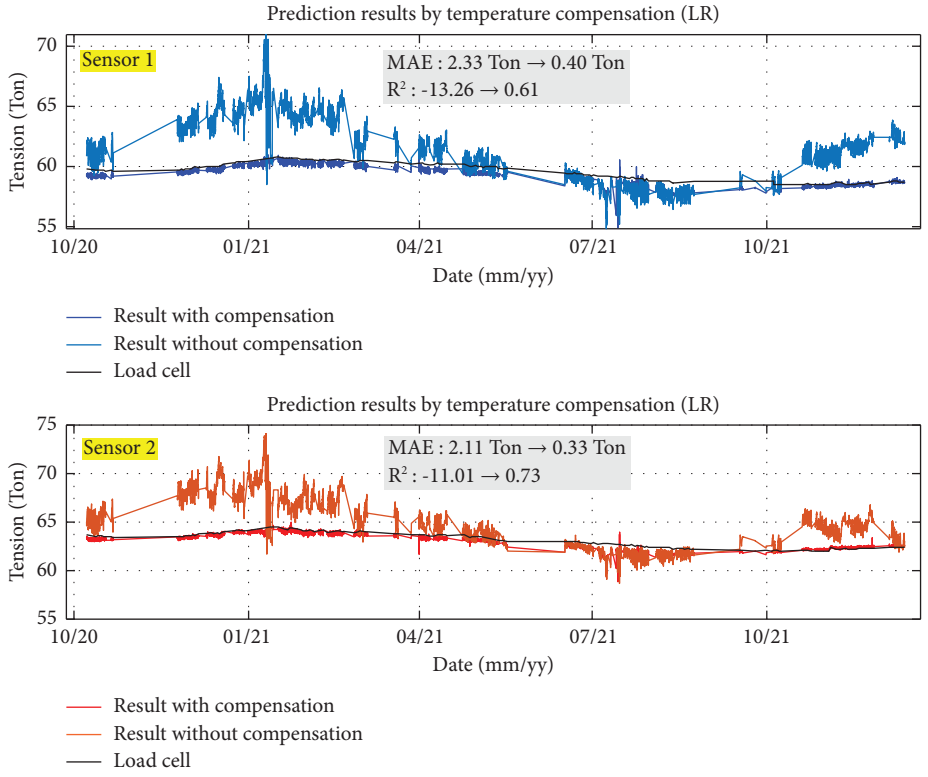

Figure 15: Tension prediction results by LR using area after temperature compensation.

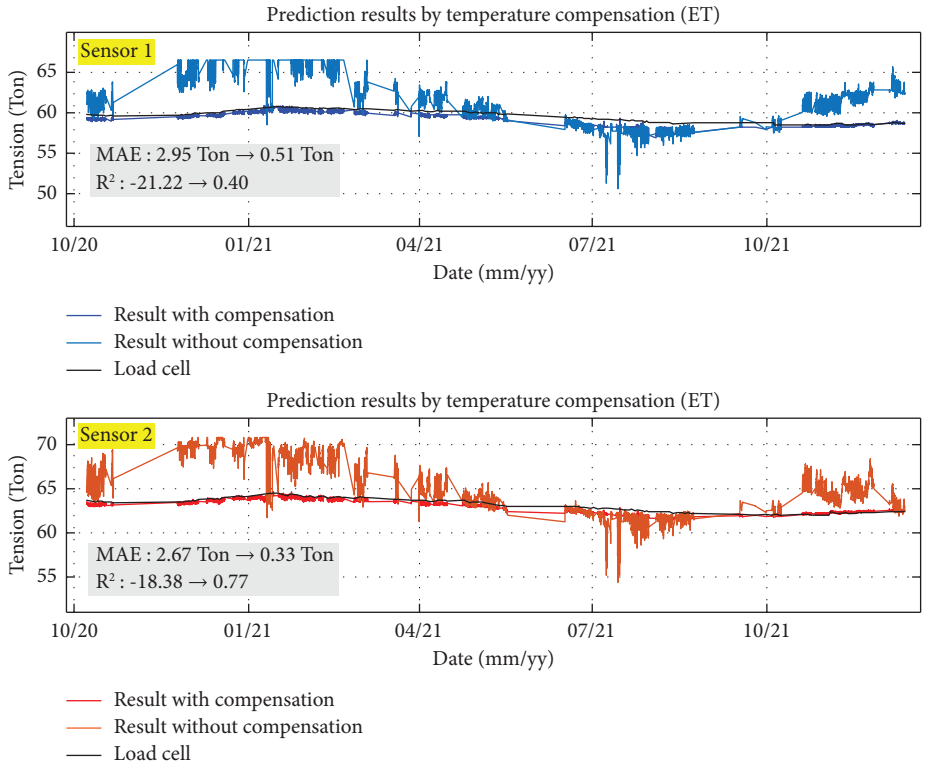

Figure 16: Tension prediction results by ET using area after temperature compensation.

Table 4: Tension prediction errors and R^2 before and after temperature compensation.

Category	Sensor 1				Sensor 2			
	LR		ET		LR		ET	
	MAE (tons)	R^2	MAE (tons)	R^2	MAE (tons)	R^2	MAE (tons)	R^2
Area	2.3285, 0.4037	−13.2643, 0.6082	2.9496, 0.5092	−21.2236, 0.4044	2.1148, 0.3296	−11.0107, 0.7252	2.6735, 0.3281	−18.3785, 0.7687
Permeability	1.6635, 0.1779	−7.2918, 0.8980	2.9293, 0.2346	−19.9320, 0.8425	1.6991, 0.1849	−7.1789, 0.9049	1.7632, 0.1888	−9.0982, 0.9125
Coercivity	8.6063, 1.2110	−182.8032, −2.6593	4.8027, 1.6453	−46.2693, −6.2060	21.3243, 3.4796	−1123.5, −34.3742	7.6549, 3.4485	−110.7544, −37.7362
Retentivity	0.9248, 0.4544	−1.0296, 0.4520	1.1091, 0.5202	−1.9763, 0.2798	1.0204, 0.3547	−1.8908, 0.7044	1.2732, 0.3705	−4.1167, 0.6772

Note. A pair of values represents before and after temperature compensation.

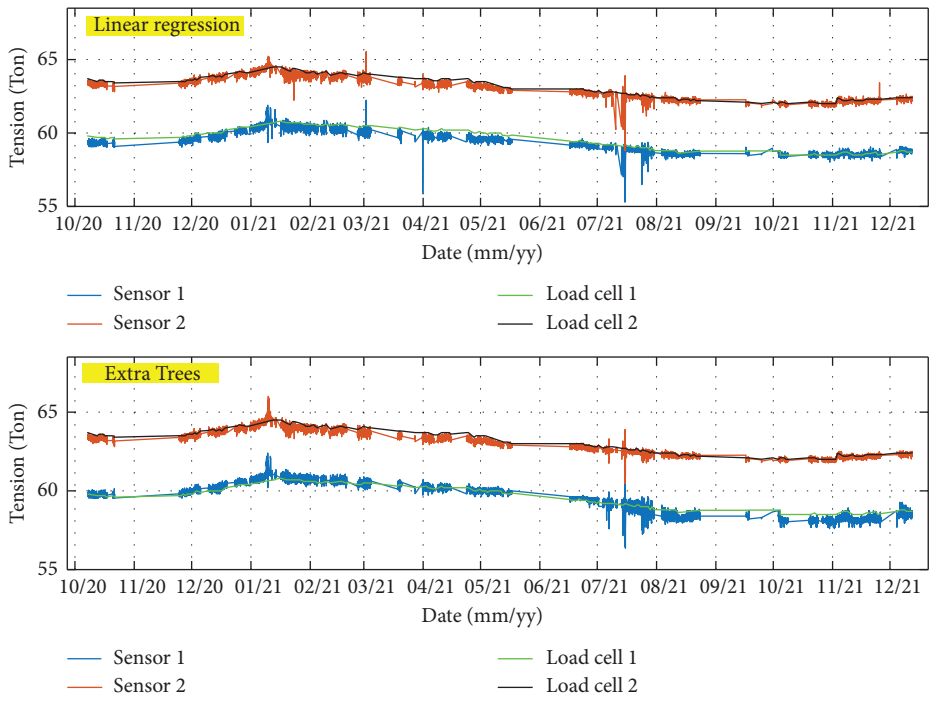

Figure 17: Prediction results by LR and ET using permeability.

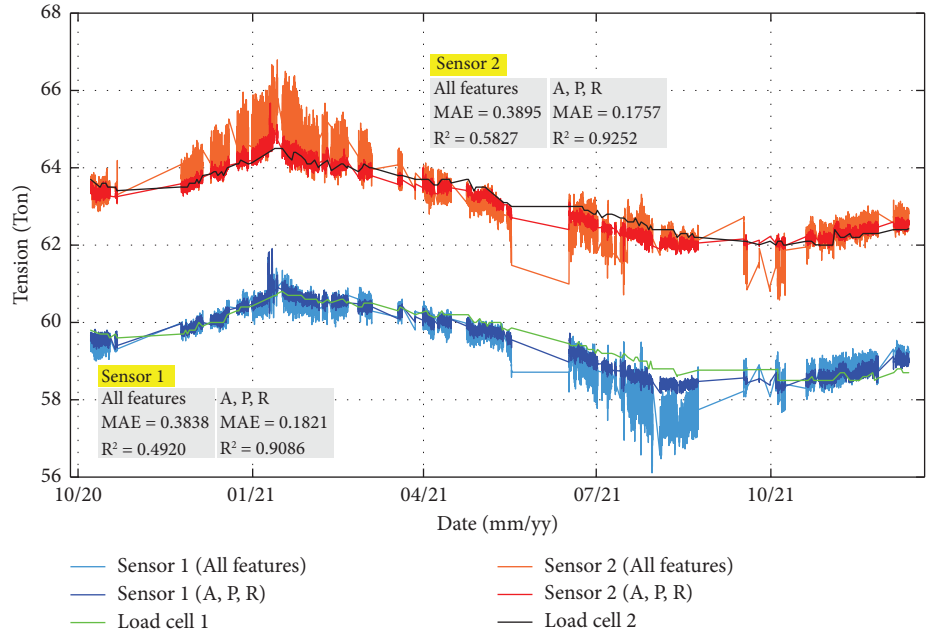

Figure 18: Tension prediction by ET (all features vs. area (A), permeability (P), and retentivity (R)).

MAE was compared and sorted as an evaluation metric. As a result of the comparison, decision-tree-based ML models such as ET, RF, and GBR were derived as the top three models. The performance of other models was found to be relatively worse in validation and test results than the aforementioned three models (i.e., in the case of CatBoost, the MAE was 0.0422 tons for sensor 1 and 0.0440 tons for sensor 2; for Ridge, the MAE was 0.0585 tons for sensor 1 and 0.0601 tons for sensor 2) while maintaining the same performance ranking regardless of training with a single feature or all features. The performances with tuned hyperparameters of the three models are shown in Table 3. The derived hyperparameters were the same for the two sensors, and the performance did not improve despite further hyperparameter tuning using the Bayesian search algorithm in all the three models. More specifically, in the optimization results using the RF, despite the trial to construct a robust model resistant to overfitting by

considering randomness through bootstrapping, the performance was not superior compared to the ET model. Furthermore, in the results of GBR, despite considering the greater complexity of the model by setting a lower threshold for impurity decrease and increasing the number of decision trees, the performance did not improve. Therefore, it can be inferred that the tension and features from EM sensor data do not form a complex relationship that is close to linear, as confirmed in the previous full-scale test.

As a result of cross-validation and testing, the ET was selected as the model for tension prediction because it had the lowest MAE with the highest R^2 among the three models. The results of the tension prediction during the monitoring period before and after temperature compensation were compared using the area of the hysteresis curve as an example of input for both LR and the ET in Figures 15 and 16.

The MAE for each algorithm was within 3 tons, and it decreased by 87.73% after temperature compensation. In both results, R^2 was negative before the compensation, which means that the used data are hard to be used for the prediction. However, the R^2 was converted into a positive number after compensation, showing that the area of the hysteresis curve became related to the tension. In addition, Table 4 presents a numerical comparison of the performance of LR and ET when all individual features were included as inputs to the prediction model.

The optimal feature was the retentivity, which exhibited the lowest MAE with the highest R^2 for both sensors. However, the prediction performances of both models changed in the order of permeability, area, retentivity, and coercivity. Moreover, the LR prediction results exhibited a better R^2 than ET for most cases. However, in the case of coercivity, the R^2 was negative even after temperature compensation. As shown in the theoretical background of the magnetic hysteresis and by the analysis of the full-scale test results, the coercivity is directly related to the magnetizing field affected by temperature and most of the change was canceled during the temperature compensation. Thus, it was found that the coercivity cannot be utilized for the tension prediction in both LR and ET algorithm as it may deteriorate the prediction result. The prediction results using the LR and the ET algorithm are shown in Figure 17 when permeability was input to both models, as it showed the best results among all features.

Meanwhile, it is possible to create a prediction model that reflects various data characteristics using ML, and it is necessary to attempt tension prediction by using several features simultaneously in the magnetic hysteresis curve. The applicability of hysteresis curve features to tension prediction could be examined by comparing the differences in results between the case using all the features of the hysteresis curve and the case using three features, except for the coercivity, which had poor relevance to the tension. Figure 18 shows the comparison results.

When the tension was predicted using each feature in ML, the error in the case of coercivity was higher than that in other cases; in particular, R^2 was a negative number, showing almost no relevance to tension. When all features were inputted into the ET model, the error increased compared to a few cases using only one feature for prediction in Table 4. However, MAE was lower, and R^2 was higher when coercivity was excluded as the input for the ET model. Therefore, a robust model can be developed for tension prediction if training and prediction are performed after excluding the feature that shows undesirable performances in the magnetic hysteresis curve.

4. Conclusion

This paper proposed a temperature compensation method for EM sensor data. Furthermore, it analyzed the field applicability of the tension prediction algorithm by comparing LR and ML algorithms during long-term monitoring. EM sensors for measuring the magnetic hysteresis of temporary steel rods were embedded inside the pier table of the Jusangcheon Bridge, a bridge under construction in Buan-gun, Jeollabuk-do, South Korea, using FCM.

For field applications, the necessity of removing temperature effects in data postprocessing during long-term monitoring has been highlighted. Therefore, a compensation method for the effects of temperature on sensor signals was proposed by conducting full-scale and field tests. Temperature compensation was successfully performed by isolating only the differences in the signals caused by tension in the temporary steel rods, showing that the estimated errors were approximately six times larger than those without temperature compensation. Subsequently, the tensions of the temporary steel rods were predicted after selecting the appropriate algorithms by adopting PyCaret open library: LR as a simple data fitting method and ET as an ML method. The results of both algorithms were compared using the evaluation metrics MAE and R^2. The results showed that the prediction capability of LR surpassed that of ML. However, as the coercivity that showed a negative R^2 was found to be sufficiently not relevant to the tension, the prediction, except for the coercivity, needed to be performed. As a result, it was observed that the prediction accuracy of ML improved as much as that of LR.

The results of the field application showed that the embedded EM sensor has good durability as it can withstand harsh conditions where the temperature fluctuates daily. However, for long-term monitoring, the prediction results indicated that the tension could not be estimated correctly unless the signal was compensated according to the variation in temperature. Prediction without temperature compensation even could reverse the trend of feature such as permeability, which shows the highest correlation with tension. Additionally, the relation between the tension and each feature of the magnetic hysteresis curve is fairly linear, indicating that LR performs better in prediction than the ML model. However, it was revealed that when using selective features for training and prediction, tension is capable of deriving results comparable to those of LR.

Data Availability

Due to privacy and ethical concerns, neither the data nor its source code can be made available to the public.

Conflicts of Interest

The authors declare that they have no conflicts of interest.

Acknowledgments

This work was supported by the Technology Development Program (S3174912) funded by the Ministry of SMEs and Startups (MSS, Korea) and a National Research Foundation of Korea (NRF) grant funded by the Korean government (MSIT) (NRF-2021R1A4A3033128).

References

[1] G. Park, *Collapse of Chilsan Bridge Caused Six Construction Workers Injured*, The Hankook Ilbo, Seoul, South Korea, 2016.

[2] H. Zui, T. Shinke, and Y. Namita, "Practical formulas for estimation of cable tension by vibration method," *Journal of Structural Engineering*, vol. 122, no. 6, pp. 651–656, 1996.

[3] S. Cho, J. P. Lynch, J. J. Lee, and C.-B. Yun, "Development of an automated wireless tension force estimation system for cable-stayed bridges," *Journal of Intelligent Material Systems and Structures*, vol. 21, no. 3, pp. 361–376, 2010.

[4] B. H. Kim and T. Park, "Estimation of cable tension force using the frequency-based system identification method," *Journal of Sound and Vibration*, vol. 304, no. 3-5, pp. 660–676, 2007.

[5] S.-H. Sim, J. Li, H. Jo et al., "A wireless smart sensor network for automated monitoring of cable tension," *Smart Materials and Structures*, vol. 23, no. 2, Article ID 025006, 2014.

[6] Y. Bao, Z. Shi, J. L. Beck, H. Li, and T. Hou, "Identification of time-varying cable tension forces based on adaptive sparse time-frequency analysis of cable vibrations," *Structural Control and Health Monitoring*, vol. 24, no. 3, Article ID e1889, 2017.

[7] A. B. Mehrabi and S. Farhangdoust, "A laser-based non-contact vibration technique for health monitoring of structural cables: background, success, and new developments," *Advances in Acoustics and Vibration*, vol. 2018, Article ID 8640674, 13 pages, 2018.

[8] W. Zhao, G. Zhang, and J. Zhang, "Cable force estimation of a long-span cable-stayed bridge with microwave interferometric radar," *Computer-Aided Civil and Infrastructure Engineering*, vol. 35, no. 12, pp. 1419–1433, 2020.

[9] D. Jana and S. Nagarajaiah, "Computer vision-based real-time cable tension estimation in Dubrovnik cable-stayed bridge using moving handheld video camera," *Structural Control and Health Monitoring*, vol. 28, no. 5, 2021.

[10] D. Jana, S. Nagarajaiah, and Y. Yang, "Computer vision-based real-time cable tension estimation algorithm using complexity pursuit from video and its application in Fred-Hartman cable-stayed bridge," *Structural Control and Health Monitoring*, vol. 29, no. 9, 2022.

[11] J.-M. Kim, H.-W. Kim, Y.-H. Park, I.-H. Yang, and Y.-S. Kim, "FBG sensors encapsulated into 7-wire steel strand for tension monitoring of a prestressing tendon," *Advances in Structural Engineering*, vol. 15, no. 6, pp. 907–917, 2012.

[12] T.-C. Huynh and J.-T. Kim, "RBFN-based temperature compensation method for impedance monitoring in pre-stressed tendon anchorage," *Structural Control and Health Monitoring*, vol. 25, no. 6, Article ID e2173, 2018.

[13] M. L. Wang, G. Wang, and Y. Zhao, "Application of EM stress sensors in large steel cables," in *Sensing Issues in Civil Structural Health Monitoring*, F. Ansari, Ed., pp. 145–154, Springer, Berlin, Germany, 2005.

[14] J. Kim, J.-W. Kim, and S. Park, "Investigation of applicability of an embedded EM sensor to measure the tension of a PSC girder," *Journal of Sensors*, vol. 2019, Article ID 2469647, 12 pages, 2019.

[15] J. Kim and S. Park, "Field applicability of a machine learning-based tensile force estimation for pre-stressed concrete bridges using an embedded elasto-magnetic sensor," *Structural Health Monitoring*, vol. 19, no. 1, pp. 281–292, 2020.

[16] O. Perevertov and R. Schäfer, "Influence of applied tensile stress on the hysteresis curve and magnetic domain structure of grain-oriented Fe–3%Si steel," *Journal of Physics D: Applied Physics*, vol. 47, no. 18, Article ID 185001, 2014.

[17] D. Singh, F. Martin, P. Rasilo, and A. Belachen, "Magneto-mechanical model for hysteresis in electrical steel sheet," *IEEE Transactions on Magnetics*, vol. 52, no. 11, pp. 1–9, 2016.

[18] W.-K. Kim, J. Kim, J. Park, J.-W. Kim, and S. Park, "Verification of tensile force estimation method for temporary steel rods of FCM bridges based on area of magnetic hysteresis curve using embedded elasto-magnetic sensor," *Sensors*, vol. 22, no. 3, p. 1005, 2022.

[19] J. Yim, M. L. Wang, S. W. Shin et al., "Field application of elasto-magnetic stress sensors for monitoring of cable tension force in cable-stayed bridges," *Smart Structures and Systems*, vol. 12, no. 3_4, pp. 465–482, 2013.

[20] R. Zhang, Y. Duan, Y. Zhao, and X. He, "Temperature compensation of elasto-magneto-electric (EME) sensors in cable force monitoring using BP neural network," *Sensors*, vol. 18, no. 7, p. 2176, 2018.

[21] M. Flah, I. Nunez, W. Ben Chaabene, and M. L. Nehdi, "Machine learning algorithms in civil structural health monitoring: a systematic review," *Archives of Computational Methods in Engineering*, vol. 28, no. 4, pp. 2621–2643, 2021.

[22] K. Bian and Z. Y. Wu, "Data-based model with EMD and a new model selection criterion for dam health monitoring," *Engineering Structures*, vol. 260, Article ID 114171, 2022.

[23] M. Y. Cheng, M. T. Cao, and P. K. Tsai, "Predicting load on ground anchor using a metaheuristic optimized least squares support vector regression model: a Taiwan case study," *Journal of Computational Design and Engineering*, vol. 8, no. 1, pp. 268–282, 2021.

[24] S. Sumitro, S. Kurokawa, K. Shimano, and M. L. Wang, "Monitoring based maintenance utilizing actual stress sensory technology," *Smart Materials and Structures*, vol. 14, no. 3, pp. S68–S78, 2005.

[25] D. C. Jiles and L. Li, "A new approach to modeling the magnetomechanical effect," *Journal of Applied Physics*, vol. 95, no. 11, pp. 7058–7060, 2004.

[26] J. Makar and B. K. Tanner, "The effect of plastic deformation and residual stress on the permeability and magnetostriction of steels," *Journal of Magnetism and Magnetic Materials*, vol. 222, no. 3, pp. 291–304, 2000.

[27] Z. Birčáková, P. Kollár, M. Jakubčin, J. Füzer, R. Bureš, and M. Fáberová, "Reversible and irreversible magnetization processes along DC hysteresis loops of Fe-based composite

materials," *Journal of Magnetism and Magnetic Materials*, vol. 483, pp. 183–190, 2019.

[28] D. C. Jiles and D. L. Atherton, "Theory of ferromagnetic hysteresis," *Journal of Magnetism and Magnetic Materials*, vol. 61, no. 1-2, pp. 48–60, 1986.

[29] R. G. Cui, S. H. Li, Z. Wang, and X. Wang, "A modified residual stress dependent Jile-Atherton hysteresis model," *Journal of Magnetism and Magnetic Materials*, vol. 465, pp. 578–584, 2018.

[30] S. H. Zhang, J. T. Zhou, H. Zhang, L. Liao, and L. Liu, "Influence of cable tension history on the monitoring of cable tension using magnetoelastic inductance method," *Structural Health Monitoring*, vol. 20, no. 6, pp. 3392–3405, 2021.

[31] X. Yang and W. Lin, "Thermistor," in *Encyclopedia of Engineering Geology. Encyclopedia of Earth Sciences Series*, P. Bobrowsky and B. Marker, Eds., Springer, Cham, 2017.

[32] J. H. Dellinger, "The temperature coefficient of resistance of copper," *Journal of the Franklin Institute*, vol. 170, no. 3, pp. 213–216, 1910.

[33] P. Refaeilzadeh, L. Tang, and H. Liu, "Cross-validation," in *Encyclopedia of Database Systems*, L. Liu and M. T. ÖZSU, Eds., pp. 532–538, Springer, Boston, 2009.

[34] S. Jasper, L. Hugo, and P. A. Ryan, "Practical Bayesian optimization of machine learning algorithms," *Advances in Neural Information Processing Systems*, vol. 25, pp. 2951–2959, 2012.